Analytical and numerical study of a circular cavity subjected to plane and cylindrical P-wave scattering

M. Tao[a], H.T. Zhao[a], Z.W. Li[a], J.B. Zhu[b],*

[a] *School of Resources and Safety Engineering, Central South University, Changsha, Hunan, China*
[b] *State Key Laboratory of Hydraulic Engineering Simulation and Safety, School of Civil Engineering, Tianjin University, Tianjin, China*

ABSTRACT

Dynamic stress concentration has been widely considered as an important factor that dominates the damage of underground cavities. To obtain the influence of wavefront curvature on the dynamic response around the circular cavity, the dynamic stress concentration near the cavity caused by the plane *P*-wave and cylindrical *P*-wave scattering is investigated based on the wave function expansion methods and Fourier transform. A three-dimensional numerical finite element model is subsequently established to simulate the dynamic damage and its influencing factors, including the period t_0 of the incident wave and the initial lateral pressure coefficient γ, around the underground cavity subjected to plane *P*-wave and cylindrical *P*-wave. The results indicate that an obvious dynamic stress concentration occurs around the cavity under dynamic stress disturbance. The dynamic stress concentration factors (DSCFs) caused by the cylindrical *P*-wave is larger than that caused by the plane *P*-wave, and the obvious tensile stress concentration, which is equivalent to the compressive stress concentration, only occurs under the cylindrical *P*-wave. Furthermore, the failure characters of the cavity under different initial static stresses and dynamic incident loadings are simulated using the multiphysics software LS-DYNA, indicating that the dynamic failures are related to the initial static pressure coefficients, period of incident wave, and incident wavefront curvature. The plastic failure under the plane *P*-wave appears initially at the compressive concentration areas while the initial failure caused by the cylindrical *P*-wave occurs at the tensile concentration areas.

1. Introduction

With the development of underground spaces and the massive exploitation of underground resources, a number of deep cavities and roadways such as those for hydropower projects, subways, and mining roadways have been constructed. However, the frequency of occurrence of dangerous and unpredicted events in underground engineering are also increasing gradually owing to complicated geological environments, high geostresses, and stress disturbances such as those arising from earthquake, unloading, blasting, and mining (Jeon et al., 2004; Li et al., 2014; Lu et al., 2012; Yan et al., 2018; Yang et al., 2016, 2013). For instance, the intensive rockbursts triggered by blasting in the vicinity of a tunnel face that occurred in the Jinping II hydropower station, China (Feng et al., 2015; Su et al., 2017). The typical spalling failure can be observed in the Baihetan hydropower station, China owing to the stress disturbance induced by excavation (Jiang et al., 2013; Xiao et al., 2016). The earthquakes in Los Angeles, Taiwan, and Wenchuan have resulted in significant damages to water and power pipeline systems and mountain tunnels buried under the surface (Hauksson and Jones, 1989; Wang et al., 2001, 2009). According to these phenomena, we found that most of them belong to dynamic disasters that can be generally interpreted as the result of the scattering of stress wave around the excavation. Therefore, the investigation of the scattering mechanism of the stress waves around the underground excavation is an important prerequisite for the construction and utilisation of underground space as well as resource exploitation.

Stress wave scattering, first proposed by Sezawa in 1927, was considered as a stress concentration phenomenon while the stress wave passes through the geometric discontinuity (Sezawa, 1927). In 1973, Pao and Mow (1973) obtained mathematical solutions for the scattering of *P*-waves around circular holes and spherical holes. In recent decades, the stress wave scattering theory has been applied gradually to geotechnical engineering and earthquake engineering. Meanwhile, numerous works on dynamic stress concentration in the vicinity of a cavity have been completed by scholars (Pao and Mow, 1993). Liu et al. (2013) proposed a new analytical method for stress wave scattering in
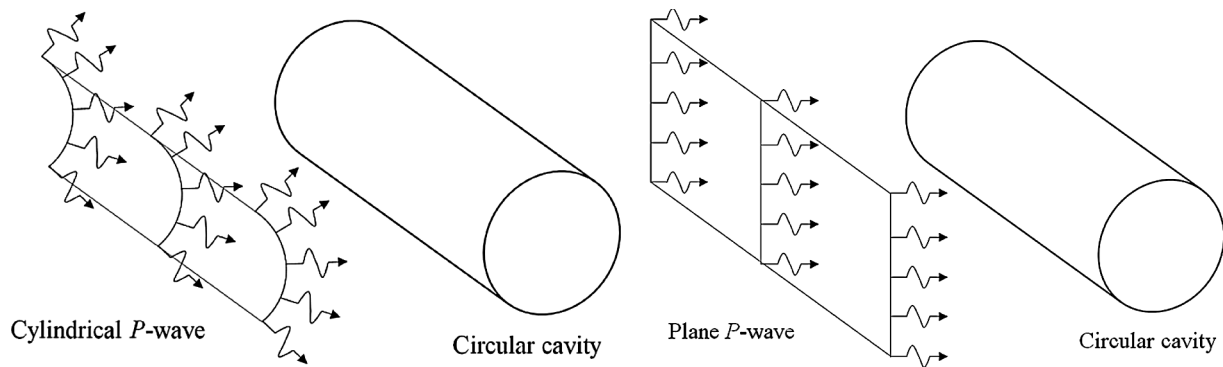

Fig. 1. Diagram of cylindrical *P*-wave and plane *P*-wave.

view of the plane complex variable theory and the image technique, and further studied the dynamic stress concentration around a shallow lined tunnel embedded in an elastic half plane under the harmonic plane *P*, *SV,* and Rayleigh waves. Mi and Kouris (2013) utilized the displacement potentials and coherent surface model to study the dynamic stress concentration in the vicinity of a nanovoid located in a semi-infinite substrate through, indicating that the dynamic stress concentration near the nanovoid is highly localised and decays rapidly. The wave function expansion method was employed by Yi et al. (2014, 2016) to investigate the DSCFs of around a circular lined tunnel with an imperfect interface subjected to cylindrical as well as plane waves using. Their results indicated that the DSCFs can be affected by the frequency of the incident wave, bonding conditions, and distance between wave source and tunnel. Zou et al. (2018) used the semi-analytical procedure to study the internal forces of a circular tunnel with imperfect interface bonding in layered ground under the plane *P* and *SV* waves, indicating that the incident angle and imperfect bonding ratio would influence the stress state of the free field owing to the stress wave scattering. Kouretzis et al. (2014) calculated the tunnel liner forces induced by compressional seismic *P*-waves using the closed-form solutions indicating that *P*-waves could lead to a significant axial hoop stress that was higher than the corresponding forces owing to shear *S*-wave incidence. Wang et al. (2014) investigated the dynamic response of a tunnel subjected to *P*-waves and *S*-waves using the dynamic finite element analysis, and their results indicated that the dynamic stress increment could be affected by both the tunnel depth and wavelength of the incident wave. Yang et al. (2017) obtained the dynamic stress concentration in an exponentially inhomogeneous plane with a circular cavity. They found that the DSCFs increased with increasing inhomogeneous parameters and fluctuated when the wave number increased to a certain value. More recently, the scattering of *P*-wave around the lined tunnel in the saturated poroelastic medium was also investigated by Fang and Jin (2017) and Liu et al. (2017). Their findings indicated that the porosity of the surrounding medium has a significant influence on DSCFs. Furthermore, Fang et al. (2015) indicated that the interaction of adjacent tunnels could enhance the imperfect interface effects. Tao et al. (2019) obtained stress redistribution of a circular cavity caused by stress wave with an arbitrary waveform, indicating that DSCFs was affected by the location of wave peak.

In addition, numerical simulation is an economical and efficient technique for simulating geotechnical and dynamic engineering problems with the rapid development of computer technology (Jing, 2003; Zhu et al., 2018). Based on these numerical analysis methods, some macroscopic and microscopic phenomena induced by stress scattering in actual engineering projects can be reconstructed, and accurate numerical solutions can be obtained quickly that is otherwise time consuming and difficult from theoretical calculations. Zhu et al. (2010) studied the rockbursts and failure modes of underground excavation located at different depths triggered by stress disturbance. Deng et al. (2014) investigated explosion and shock wave propagation in an

underground rock opening and dynamic responses of a tunnel using the FEM-DEM hybrid method. Li and Weng (2016) studied the dynamic behaviours in the vicinity of the underground excavation though the LS-DYNA. Wang and Cai (2015) analysed the influence of incident wavelength on the dynamic response around the opening with different sizes and shapes using the seismic wave propagation modelling software SPECFEM2D. Huang et al. (2017) studied the seismic response of tunnels under obliquely incident P waves in view of ABAQUS, indicating that the most serious damage appears at the tunnel crossing the fault. Li et al. (2018) obtained the dynamic response and energy evolution of the deep-buried tunnels subjected to blasting loads based on PFC2D. Liu et al. (2018a,b) studied the characters of stress wave scattering and dynamic stress concentration around the spherical cavity in an infinite domain based on theoretical analysis and numerical simulation, indicating that the dynamic response depended strongly on the incident wave frequency, medium porosity, and boundary drainage condition. Moreover, Zhu et al. (2014) used COMSOL to study the dynamic stress distribution and resultant damage zone near the underground excavation owing to transient unloading. Li et al. (2016) investigated the vibration velocity, deformation, and maximum principle stress caused by transient unloading in the adjacent tunnels using FLAC3D. However, most of the works concentrate primarily on the dynamic response caused by plane *P*-waves rather than cylindrical *P*-waves, and few studies have focused on the influence of incident wavefront curvature. In fact, the incident wavefront varies with the distance from the wave source to the cavities r_0, and the size of the cavities *a*. When the incident wavefront curvature relative to the cavity is large, the incident stress wave can be regarded as a cylindrical *P*-wave, and it can be approximated as a plane *P*-wave when the incident wavefront curvature relative to the cavity is small, as shown in Fig. 1. Therefore, it is necessary to further explore the influence of wavefront curvature on the dynamic response induced by stress scattering.

The primary objective of this study is to investigate the transient response of a circular cavity subjected to both plane and cylindrical *P*-wave scattering, and to further study the influence of incident wavefront curvature based on theoretical analysis and numerical simulation. The process of dynamic stress concentration and dynamic failures around the circular cavity under plane *P*-wave and cylindrical *P*-wave with different period are analysed. In addition, the initial geostress and lateral pressure coefficients γ are considered. The results indicate that the distribution and stress concentration level can be affected by the wavefront curvature of the incident wave. The cylindrical P-wave can be approximated as a plane *P*-wave when the distance from the wave source to the cavity is larger than 10*a*.

2. Scattering theory of stress wave around circular hole

A time-varying incident *P*-wave propagates perpendicularly to the normal direction of the plane where the hole is located. The plane *P*-wave is generally considered as the wave generated by a line source at

infinity, and the incident P-wave $\varphi_{PP}^{(i)}$ can be expressed at the centre of the circular cavity (r, θ) as (Pao and Mow, 1993)

$$\varphi_{PP}^{(i)} = \varphi_0 e^{i(\alpha x - \omega t)} \tag{1}$$

The cylindrical P-wave is generated from the line source at $(\bar{r}, \bar{\theta})$, and the wavefront curvature will change with the distance between source $(\bar{r}, \bar{\theta})$ and the centre of the circular cavity (r, θ). Therefore, to investigate the effects of wavefront curvature on stress wave scattering around the cavity, the incident cylindrical P-wave should be expressed at the polar coordinates $(\bar{r}, \bar{\theta})$, as follows (Pao and Mow, 1993)

$$\varphi_{PC}^{(i)} = \varphi_0 H_0^{(1)}(\alpha \bar{r}) e^{-i\omega t} \tag{2}$$

Through the coordinate transformation and wave function expansion methods, Eqs. (1) and (2) can be further expressed at the co-ordinate (r, θ) as

$$\varphi_{PP}^{(i)} = \varphi_0 \sum_{n=0}^{\infty} \varepsilon_n (i)^n J_n(\alpha r) \cos n\theta e^{-i\omega t} \tag{3}$$

$$\varphi_{PC}^{(i)} = \varphi_0 \sum_{n=0}^{\infty} (-1)^n \varepsilon_n J_n(\alpha r) H_n^{(1)}(\alpha r_0) \cos n\theta e^{-i\omega t} \tag{4}$$

where $\varepsilon_n = \begin{cases} 1, & n = 0 \\ 2, & n \geqslant 1 \end{cases}$; φ_0 is the amplitude of the incident wave; α is the wave number; ω is the circular frequency; $J_n(\alpha r)$ and $H_n^{(1)}(\alpha r_0)$ are the first Bessel function and Hankel function, respectively.

When the incident P-wave reaches the periphery of the circular hole, stress scattering occurs around the circular hole to generate new P-waves and SV waves (Li et al., 2016; Tao et al., 2018). They can be expressed as

$$\varphi_P^{(r)} = \sum_{n=0}^{\infty} A_n H_n^{(1)}(\alpha r) \cos n\theta e^{-i\omega t} \tag{5}$$

$$\psi_{SV}^{(r)} = \sum_{n=0}^{\infty} B_n H_n^{(1)}(\beta r) \sin n\theta e^{-i\omega t} \tag{6}$$

where $\beta = \omega / C_s$ is the wave number of the shear wave; C_s is the shear wave velocity in the rock mass; A_n and B_n are the undetermined coefficients. Therefore, the scattering of the incident stress wave as well as the influence of the derivative wave must be considered. According to the superposition principle of the elastic wave, the total wave of plane P-waves cylindrical P-waves, and SV waves acting on the circular hole can be respectively written as

$$\varphi_{PP} = \sum_{n=0}^{\infty} [\varphi_0 \varepsilon_n (i)^n J_n(\alpha r) + A_n H_n^{(1)}(\alpha r)] \cos n\theta e^{-i\omega t} \tag{7}$$

$$\varphi_{PC} = \sum_{n=0}^{\infty} [(-1)^n \varphi_0 \varepsilon_n J_n(\alpha r) H_n^{(1)}(\alpha r_0) + A_n H_n^{(1)}(\alpha r)] \cos n\theta e^{-i\omega t} \tag{8}$$

$$\psi_{SV}^{(r)} = \sum_{n=0}^{\infty} B_n H_n^{(1)}(\beta r) \sin n\theta e^{-i\omega t} \tag{9}$$

Combined with the relationship between stress and displacement potential, the stress expressions in the vicinity of a circular cavity under plane P-wave can be expressed as (Tao et al., 2018)

$$\sigma_{rr}^P = \frac{2\mu}{r^2} \sum_{n=0}^{\infty} [\varepsilon_n (i)^n \varphi_0 \varepsilon_{11}^{(1)} + A_n^P \varepsilon_{11}^{(3)} + B_n^P \varepsilon_{12}^{(3)}] \cos n\theta e^{-i\omega t} \tag{10}$$

$$\sigma_{r\theta}^P = \frac{2\mu}{r^2} \sum_{n=0}^{\infty} [\varepsilon_n (i)^n \varphi_0 \varepsilon_{41}^{(1)} + A_n^P \varepsilon_{41}^{(3)} + B_n^P \varepsilon_{42}^{(3)}] \sin n\theta e^{-i\omega t} \tag{11}$$

$$\sigma_{\theta\theta}^P = \frac{2\mu}{r^2} \sum_{n=0}^{\infty} [\varepsilon_n (i)^n \varphi_0 \varepsilon_{21}^{(1)} + A_n^P \varepsilon_{21}^{(3)} + B_n^P \varepsilon_{22}^{(3)}] \cos n\theta e^{-i\omega t} \tag{12}$$

The stress expressions around the circular cavity under cylindrical P-wave can be expressed as (Li et al., 2016)

$$\sigma_{rr}^C = \frac{2\mu}{r^2} \sum_{n=0}^{\infty} [(-1)^n \varphi_0 \varepsilon_n H_n^{(1)}(\alpha r_0) \varepsilon_{11}^{(1)} + A_n^C \varepsilon_{11}^{(3)} + A_n^C \varepsilon_{12}^{(3)}] \cos n\theta e^{-i\omega t} \tag{13}$$

$$\sigma_{r\theta}^C = \frac{2\mu}{r^2} \sum_{n=0}^{\infty} [(-1)^n \varphi_0 \varepsilon_n H_n^{(1)}(\alpha r_0) \varepsilon_{41}^{(1)} + A_n^C \varepsilon_{41}^{(3)} + B_n^C \varepsilon_{42}^{(3)}] \sin n\theta e^{-i\omega t} \tag{14}$$

$$\sigma_{\theta\theta}^C = \frac{2\mu}{r^2} \sum_{n=0}^{\infty} [(-1)^n \varphi_0 \varepsilon_n H_n^{(1)}(\alpha r_0) \varepsilon_{21}^{(1)} + A_n^C \varepsilon_{21}^{(3)} + B_n^C \varepsilon_{22}^{(3)}] \cos n\theta e^{-i\omega t} \tag{15}$$

where $\varepsilon_{11}^{(1)}$, $\varepsilon_{11}^{(3)}$, etc. are the contributions of various waves to the stresses; r is the distance to the centre of the hole; μ is the Lame constant of an elastomer. According to the mechanical theory of elasticity, the stress boundary condition for a hole with radius a at $r = a$ is $\sigma_{rr}|_{r=a} = 0$ and $\sigma_{r\theta}|_{r=a} = 0$. Therefore, the undetermined coefficients A_n^P and B_n^P under plane P-wave can be written as

$$A_n^P = -\varepsilon_n i^n \varphi_0 \frac{\begin{vmatrix} E_{11}^{(1)} & E_{12}^{(3)} \\ E_{41}^{(1)} & E_{42}^{(3)} \end{vmatrix}}{\begin{vmatrix} E_{11}^{(3)} & E_{12}^{(3)} \\ E_{41}^{(3)} & E_{42}^{(3)} \end{vmatrix}} = -\varepsilon_n i^n \varphi_0 A_n$$

$$B_n^P = -\varepsilon_n i^n \varphi_0 \frac{\begin{vmatrix} E_{11}^{(3)} & E_{11}^{(1)} \\ E_{41}^{(3)} & E_{41}^{(1)} \end{vmatrix}}{\begin{vmatrix} E_{11}^{(3)} & E_{12}^{(3)} \\ E_{41}^{(3)} & E_{42}^{(3)} \end{vmatrix}} = -\varepsilon_n i^n \varphi_0 B_n \tag{16}$$

A_n^P and B_n^P under cylindrical P-wave can be written as

$$\begin{cases} A_n^C = (-1)^{n+1} \varphi_0 \varepsilon_n H_n^{(1)}(\alpha r_0) A_n \\ B_n^C = (-1)^{n+1} \varphi_0 \varepsilon_n H_n^{(1)}(\alpha r_0) B_n \end{cases} \tag{17}$$

where $E_{11}^{(1)}$, $E_{41}^{(1)}$, $E_{21}^{(1)}$, etc. are the values of $\varepsilon_{11}^{(1)}$, $\varepsilon_{41}^{(1)}$, $\varepsilon_{21}^{(1)}$... evaluated at $r = a$. Subsequently, the distribution of stress around the hole can be obtained by substituting A_n^P, B_n^P and A_n^C, B_n^C into the stress expression of the plane P-wave and cylindrical P-wave.

To characterise the general law of varied stress around a circular hole under an arbitrary stress wave, the DSCF was employed in this study. In general, the DSCF can be expressed as the ratio of the hoop stress at any point around the circular hole to the maximum radial stress generated when the incident wave propagates in the intact medium. The maximum radial stress of the intact elastomer under a plane P-wave and cylindrical P-wave can be expressed as

$$\sigma_{PP,rr} = \mu \beta^2 \varphi_0 \tag{18}$$

$$\sigma_{PC,rr} = \alpha^2 \mu \varphi_0 [H_2^{(1)}(\alpha \bar{r}) + (1 - \kappa^2) H_0^{(1)}(\alpha \bar{r})] e^{-i\omega t} \tag{19}$$

Therefore, their DSCFs around the circular cavity can be written as

$$\sigma_{PP,\theta\theta} = \frac{\sigma_{\theta\theta}^P}{\sigma_{PP,rr}} \bigg|_{r=a} = \frac{2}{\beta^2 r^2} \sum_{n=0}^{\infty} [\varepsilon_n (i)^n (\varepsilon_{21}^{(1)} - A_n \varepsilon_{21}^{(3)} - B_n \varepsilon_{22}^{(3)})] \cos n\theta e^{-i\omega t} \tag{20}$$

$$\sigma_{PC,\theta\theta} = \frac{\sigma_{\theta\theta}^C}{\sigma_{PC,rr}} \bigg|_{r=a}$$
$$= \frac{2}{\alpha^2 r^2} \frac{\sum_{n=0}^{\infty} (-1)^n \varepsilon_n H_n^{(1)}(\alpha r_0)(\varepsilon_{21}^{(1)} - A_n \varepsilon_{21}^{(3)} - B_n \varepsilon_{22}^{(3)}) \cos n\theta}{H_2^{(1)}(\alpha \bar{r}) + (1 - \kappa^2) H_0^{(1)}(\alpha \bar{r})} \tag{21}$$

where $\bar{r} = \sqrt{a^2 + r_0^2 + 2ar_0 \cos \theta}$, a is the radius of the circular cavity, and r_0 is the distance from the wave source to the centre of the cavity.

In the previous section, theoretical analysis is only performed on the scattering of harmonic waves around the circular hole. However, the majority of disturbances exhibit obvious aperiodicity owing to the

uncertainty of the wave source and the complexity of the rock medium, belonging to the typical non-periodic loads. These types of loads are generally regarded as transient loads that can induce a transient response around the circular hole. To obtain the dynamic response of the transient disturbance, the Fourier transform is introduced to decompose the aperiodic dynamic stress wave into its harmonic component, and subsequently calculate the steady-static response according to the previous analysis (Li et al., 2016; Tao et al., 2018). The transient response of the system under an arbitrary incident function $f(t)$ can be expressed as

$$g(x_i, t) = \frac{1}{\sqrt{2\pi}} \int_{-\infty}^{\infty} X(x_i, \omega) F(\omega) e^{-i\omega t} d\omega \tag{22}$$

where $F(\omega)$ is the Fourier transform of the incident function $f(t)$; $X(x_i, \omega)$ is the admittance function that is the steady-state response of the system. The dimensionless analysis is used for simplifying the calculation, and the action time $\bar{t}$ was normalised by the time travelling through the length of a radius:

$$\bar{t} = \frac{c_p t}{a} \tag{23}$$

where c_p is the velocity of the P-wave in rock mass.

In addition, the $\delta(t)$ function and Heaviside step function are employed to reduce the computational complexity, and the Fourier transform of $\delta(t)$ function can be expressed as

$$\frac{1}{\sqrt{2\pi}} \int_{-\infty}^{\infty} \delta(t) e^{-i\omega t} dt = \frac{1}{\sqrt{2\pi}} \tag{24}$$

Therefore, the dynamic response, which is regarded as a unit impulse response caused by the $\delta(t)$ function, can be expressed as

$$g_\delta(x_i, t) = \frac{1}{2\pi} \int_{-\infty}^{\infty} X(x_i, \omega) e^{-i\omega t} d\omega \tag{25}$$

Eq. (25) indicates that the impulse response is the Fourier transform of the admittance function. Hence, the transient response of the Heaviside step function can be expressed by the impulse response as

$$g_h(x_i, t) = \frac{2}{\pi} \int_0^{\infty} \frac{X(x_i, \omega) \sin \omega x}{\omega} d\omega \tag{26}$$

According to the Duhamel integral, the transient response of an arbitrary input function $f(t)$ can be derived from

$$g(x_i, t) = \int_0^t f(\tau) g_h'(t - \tau) d\tau \tag{27}$$

In fact, most dynamic loads will first experience a short rising time to reach the peak value and subsequently decrease gradually to zero. Herein, the dynamic disturbance process is represented by a unit of a half sine wave, as shown in Fig. 2. The corresponding function can be written as

$$f(t) = \begin{cases} \sin\left(\frac{\pi t}{t_0}\right), & 0 \leqslant t < t_0 \\ 0, & t \geqslant t_0 \end{cases} \tag{28}$$

The transient response around the circular cavity can be obtained by substituting Eq. (28) into Eq. (27). When $0 \leq t < t_0$, the transient can be written as

$$g(x_i, t) = \frac{2}{\pi} \int_0^t f'(\tau) d\tau \int_0^{\infty} \frac{X(x_i, \omega) \sin \omega(t-\tau)}{\omega} d\omega$$
$$= \int_0^{\infty} \frac{X(x_i, \omega)}{\omega} \left[\frac{\cos \omega t - \cos(\pi t/t_0)}{\pi - \omega t_0} - \frac{\cos \omega t - \cos(\pi t/t_0)}{\pi + \omega t_0} \right] d\omega \tag{29}$$

When $t \geq t_0$, the transient can be written as

$$g(x_i, t) = \frac{2}{\pi} \int_0^t f'(\tau) d\tau \int_0^{\infty} \frac{X(x_i, \omega) \sin \omega(t-\tau)}{\omega} d\omega$$
$$= \int_0^{\infty} \frac{X(x_i, \omega)}{\omega} \left[\frac{\cos \omega t - \cos(\pi + \omega t - \omega t_0)}{\pi - \omega t_0} - \frac{\cos \omega t - \cos(\pi + \omega t_0 - \omega t)}{\pi + \omega t_0} \right] d\omega \tag{30}$$

From Eqs. (29) and (30), we found that the key step in solving the dynamic response around the circular cavity under transient wave
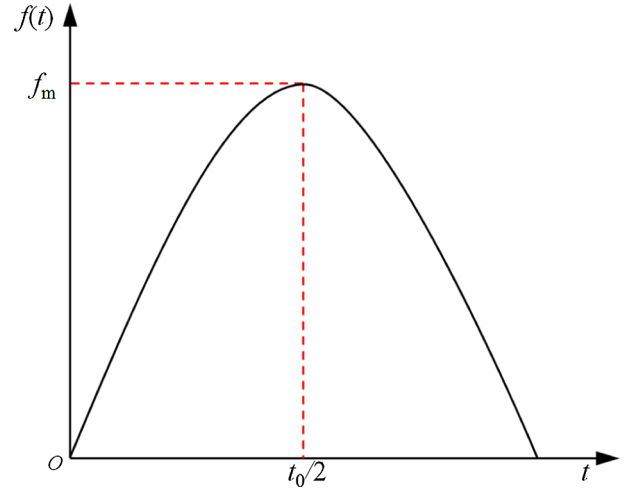

Fig. 2. Curve of dynamic disturbance.

incidence is to obtain the value of $X(x_i, \omega)$. In fact, $X(x_i, \omega)$ is the real part of the steady-state response in the vicinity of the circular cavity, which can be calculated by mathematical software. In this study, the transient response is calculated through the Mathematica because of its powerful symbolic computing capabilities. The stress and deformation energy distribution around the circular hole can be investigated.

3. Distribution characteristics of dynamic stress concentration factor

To compare and analyse the dynamic response around the circular cavity caused by a transient plane P-wave and cylindrical P-wave, the DSCFs at $\theta = 0$, $\theta = \pi/4$, and $\theta = \pi/2$ under a dynamic stress wave with different period t_0 are calculated. The direction of the incident stress wave is $\theta = \pi$ and the radius of the circular cavity is 1.0 m. The other parameters, including Young's modulus, density, and Poisson's ratio, were chosen from the rock mass, and the corresponding values are $E = 16.26 \times 10^9$ Pa, $\rho = 2620$ kg/m^{-3}, and $v = 0.25$.

The distribution of DSCFs around the circular cavity under the plane P-wave is plotted in Fig. 3(a)–(c), corresponding to the points at $\theta = 0$, $\theta = \pi/4$, and $\theta = \pi/2$. As shown in Fig. 3, the trend of the DSCFs varying with the dimensionless time $\bar{t}$ at different angles is similar to each other. Firstly, the DSCFs increase rapidly towards the positive direction and decrease rapidly after the peak values. Subsequently, it increases rapidly to the maximum value in the negative direction and finally returns to zero gradually with the increasing $\bar{t}$. This indicates that the compressive and tensile stress concentrations occur successively in the vicinity of the circular cavity when the stress wave scatters on the periphery of the cavity. At $\theta = 0$, the tensile stress concentration caused by the stress wave with a period t_0 of less than 20 is greater than the compressive stress concentration, while the opposite situation occurs when t_0 is greater than 20. In addition, the noticeable oscillation of the DSCF appears at $\theta = 0$ with the continuous increase in the dimensionless time $\bar{t}$. Further, the oscillation amplitude decreases gradually while the oscillation duration increases gradually with increasing t_0. At $\theta = \pi/4$, the compressive stress concentration factor increases significantly, while the tensile stress concentration factor decreases gradually, and the compressive stress concentration factor at $t_0 = 5$ is less than that at $t_0 = 20$. At $\theta = \pi/2$, the compressive stress concentration factor continues to increase and its maximum value at $t_0 = 20$ is 2.79; additionally, the tensile stress factor is also greater than that at $t_0 = 5$.

Fig. 4 shows the distribution of DSCFs around the circular cavity under the action of the cylindrical P-wave. The distance between wave source and circular cavity is $5a$. As shown, the DSCFs at different angles
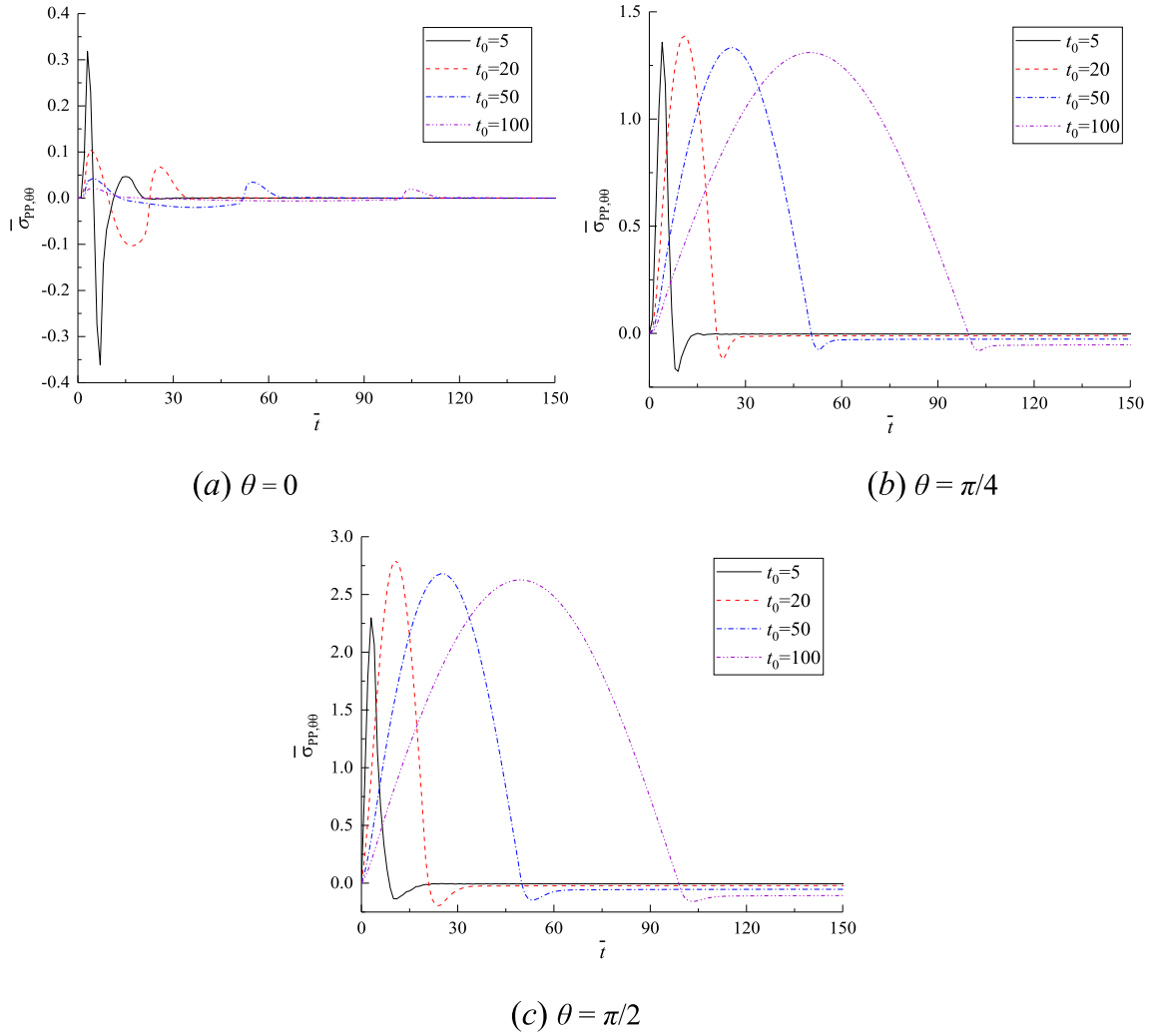
$(a)\ \theta = 0$

$(b)\ \theta = \pi/4$

$(c)\ \theta = \pi/2$

Fig. 3. Distribution of dynamic stress concentration around a circular roadway under plane *P*-waves.

exhibit an obvious variation. At $\theta = 0$, the DSCFs first increases to the peak value in the negative direction and subsequently returns to the position near zero as the dimensionless time $\bar{t}$ increases, and the DSCFs induced by the stress wave with a larger t_0 increase slightly towards the positive direction in the later period. This phenomenon indicates that the significant tensile stress concentration first occurs at $\theta = 0$ and the subsequent compressive stress concentration only occurs under the cylindrical stress wave with a larger t_0, which is significantly different from the situation of the plane *P*-wave. Furthermore, the tensile stress concentration decreases first and subsequently increases with the increase in the t_0 of the stress wave, and the maximum tensile stress concentration obtained at $t_0 = 50$ is -4.56. At $\theta = \pi/4$, the relationship between the DSCFs and dimensionless time $\bar{t}$ under the cylindrical *P*-wave is similar to that caused by the plane *P*-wave at $\theta = 0$, and the level of tensile stress concentration is greater than the compressive stress as a whole. In addition, the maximum compressive stress concentration factor occurring at $t_0 = 5$ is 0.57 in the initial stage, and the maximum tensile stress concentration at $t_0 = 20$ is -1.47. At $\theta = \pi/2$, the stress concentration corresponding to different t_0, except $t_0 = 5$, is less than that at $\theta = 0$. This illustrates that the compressive stress concentration areas are distributed at the vicinity of $\theta = \pi/2$, and most of the stress concentration levels are less than the tensile stress concentration at $\theta = 0$.

To further obtain the complete distribution characters of stress around the cavity under the plane *P*-wave and cylindrical *P*-wave, the relationship between the DSCFs and angles when the period of the

incident wave is $t_0 = 20$ and corresponding to the dimensionless times 10, 20, 30, 40, and 50 is calculated. The results are plotted in Fig. 5. As shown, the DSCFs around the cavity show the similar trends with increasing dimensionless time. The compressive stress concentration factors increase first and subsequently decrease with the increase in the dimensionless time $\bar{t}$, and the maximum compressive stress concentration level is obtained at $\bar{t} = 20$. However, the tensile stress concentration factor continues to decrease when the stress wave acts on the circular cavity, and increases gradually after the stress wave passes through the cavity. This indicates that the continuous increase in compressive stress concentration occurs primarily in the rising stage of the stress wave, while the tensile stress concentration occurs in the entire process.

The obvious differences in the stress distribution around the cavity under the action of plane and cylindrical *P*-waves can be found in Fig. 5. Under the action of the plane *P*-wave, especially during the period of stress wave passing through the roadway ($\bar{t} = 10$–40), the DSCFs are distributed symmetrically around the cavity. The compressive stress is concentrated at approximately $\theta = \pi/2$ and $\theta = 3\pi/2$, and the tensile stress concentration areas are located primarily at $\theta = 0$ and $\theta = \pi$. However, the DSCFs are no longer distributed symmetrically and the stress concentration level in the shadow side is greater than that in the illuminated side when the plane *P*-wave has just passed through the cavity ($\bar{t} = 40$). The DSCFs in the two sides of the circular roadway tend to approach zero, indicating that the roadway gradually returns to the initial stress state where no dynamic disturbance occurred. Under the
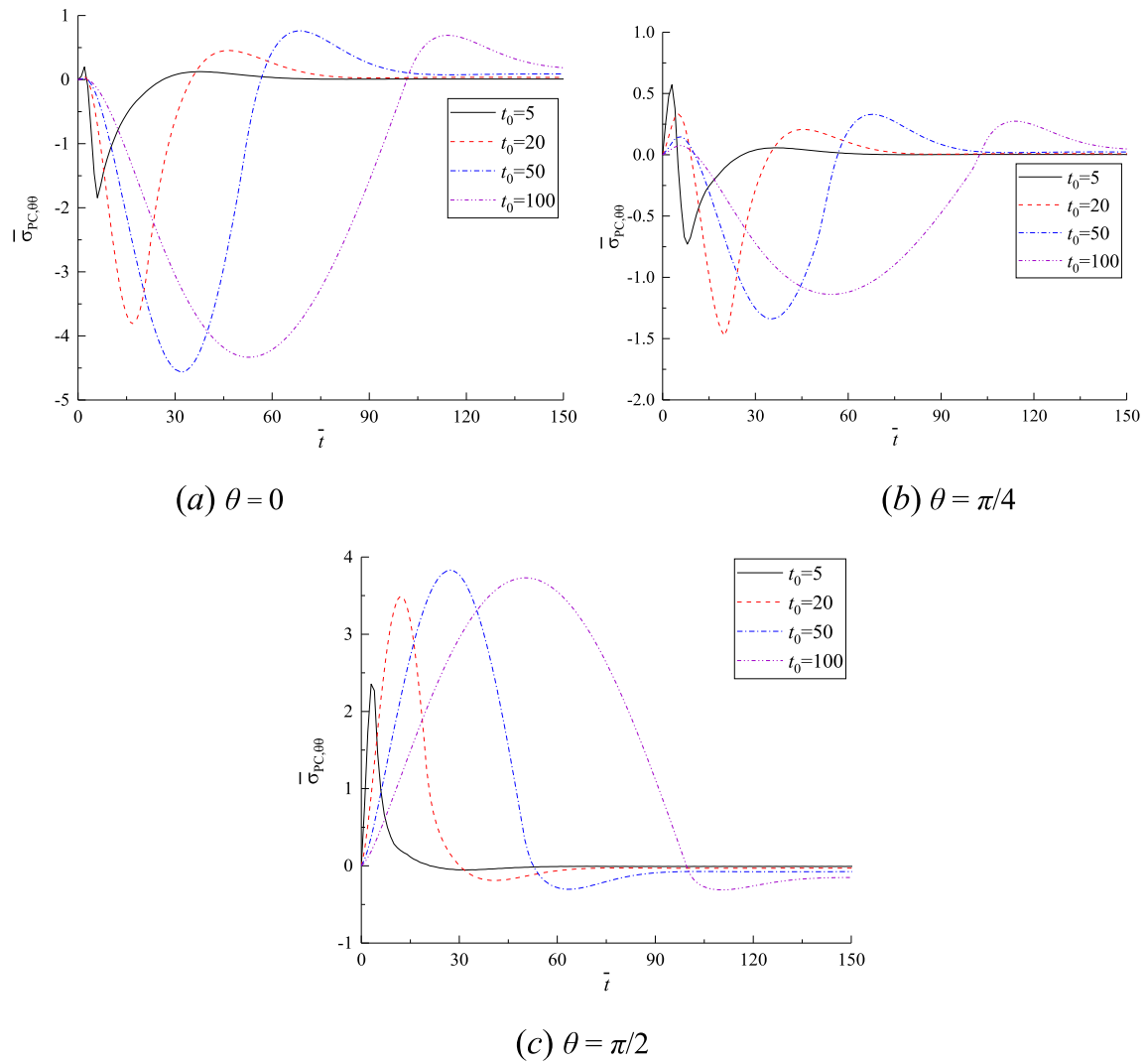
$(a)\ \theta = 0$

$(b)\ \theta = \pi/4$

$(c)\ \theta = \pi/2$

Fig. 4. Distribution of dynamic stress concentration around a circular roadway under cylindrical P-waves.

(a) Plane P-wave

(b) Cylindrical P-wave
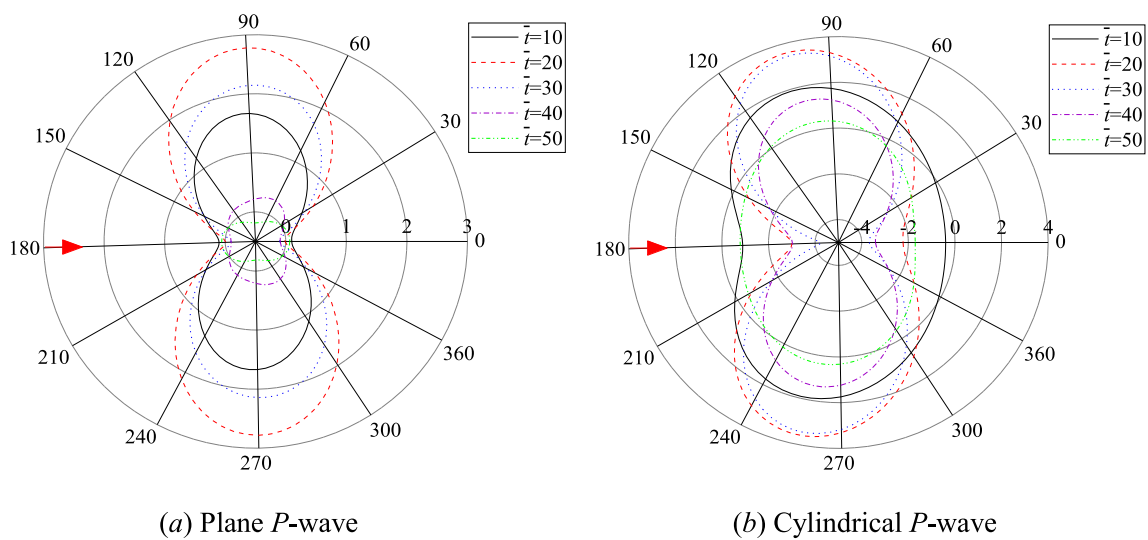
Fig. 5. Variation characters of dynamic stress concentration factor with time of stress wave.

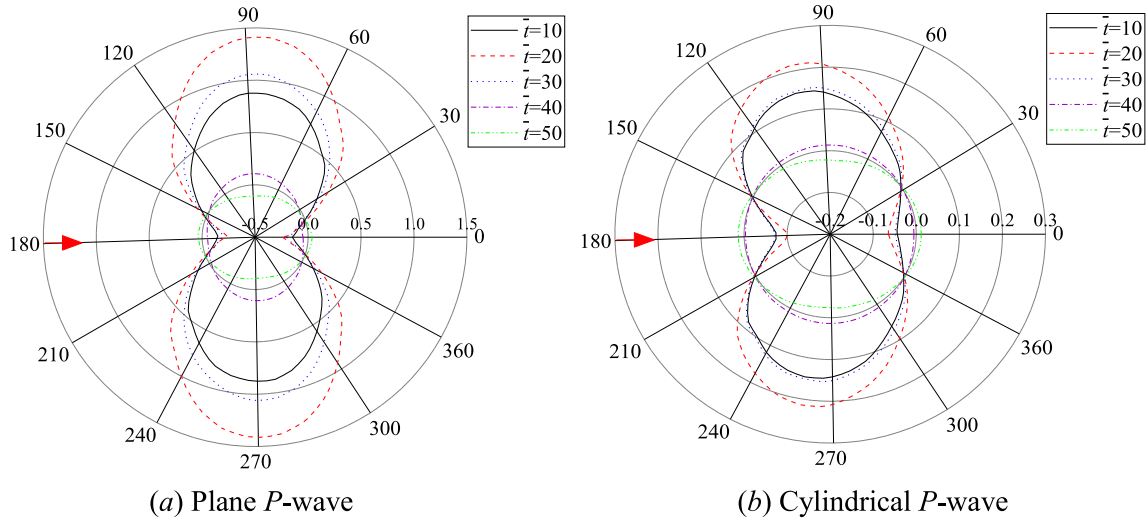(a) Plane P-wave   (b) Cylindrical P-wave

Fig. 6. Numerical simulation of dynamic stress distribution around the cavity.

action of the cylindrical P-wave, the DSCF is distributed symmetrically along the incident direction of the stress wave ($\theta = \pi$–0). The compressive stress concentration factors, distributed primarily in the range of $\theta = \pi/3$–$5\pi/6$ and $\theta = 7\pi/6$–$5\pi/3$, inclined to the illuminated side. The tensile stress occurred primarily at the vicinity of $\theta = 0$ and $\theta = \pi$, and the tensile concentration level on the shadow side is less than that on the illuminated side.

4. Numerical verification and coupled static-dynamic model

4.1. Numerical verification of the analytical solution

To verify the theoretical solution, stress wave scattering in the elastic materials with a cavity 1.0 m in radius is simulated numerically using LS-DYNA. The size of the numerical model is 30 m × 20 m × 2 m, and non-reflective boundaries are used in addition to the stress loading boundary. The dynamic stress distribution around the cavity is normalised by the amplitude of the incident pressure, as presented in Fig. 6. As shown, the variation tendencies of the dynamic stress distribution under the plane P-wave and cylindrical P-wave are similar to the theoretical results, as shown in Fig. 5. In particular, the stress level in the compressive stress concentration areas is larger than that in the tensile concentration areas under the plane P-wave, while the maximum tensile stress is extremely close to the maximum compressive stress at $\bar{t} = 20$. Meanwhile, a slight difference between the simulation and theoretical results, such as the stress level around the circular cavity under the cylindrical P-wave, is smaller than that under the plane P-wave in the simulation. Additionally, the dynamic stress in the tensile stress concentration areas varies with the dimensionless time $\bar{t}$ and is different from the numerical solution. This is because the propagation of the cylindrical wave is a divergent process that induces energy dissipation and results in the reduction in the stress level around the circular cavity. Therefore, the results verified that the theoretical solution is correct.

The previous section only considers the dynamic effect in the definition of the DSCF, which proves that the dynamic effect indeed exists. However, in practical engineering, the underground rock mass is naturally pre-stressed. Especially in deep rock engineering, the initial stress concentration appears in the periphery of the excavated tunnel owing to the action of gravitational and tectonic stresses. The concentrated stress around the excavated tunnel will further change the stress state of the surrounding rock and even form some excavation-damaged zones (Golshani et al., 2007; Labiouse and Vietor, 2014; Lisjak et al., 2014; Zhu et al., 2014). Therefore, considering the initial

geostress of the underground tunnel is necessary and significant for exploring its dynamic response. Further numerical simulations employing LS-DYNA were performed, as described in the following sections.

4.2. Material model and validation

Rock is a typical anisotropic material, and non-elastic deformations as well as failures can be computed easily when the dynamic or static loads are applied to it. Therefore, it is important to obtain a suitable material model that characterises the mechanical properties of rock. According to previous studies, the Taylor–Chen–Kuszmaul model, the Johnson–Holmquist model, and the continuous surface cap model (CSCM) are used widely to simulate the damage and fracture characters of rock materials (Tao et al., 2012). In the paper thereof, the CSCM was employed to investigate the hard-rock material because of the considered compression damage and tensile damage. The material includes the isotropic constitutive equation, shear failure criterion, hardening failure criterion, brittle failure criterion, ductile failure criterion, energy equation, and strain-rate-dependent equation of the material. Among them, the shear failure surface and compression failure surface are connected by a curved surface into a smooth yield surface that can effectively characterise the mechanical properties of brittle materials such as concrete and rock (Brannon and Leelavanichkul, 2009; Tao et al., 2012). The yield equation is expressed as (LSTC, 2007)

$$f(J_1, J_2, J_3, k) = J_2 - \mathfrak{R}^2 F_c F_f^2 \tag{31}$$

where J_1, J_2, and J_3 are the first, second, and third invariants of the stress tensor, respectively; k is the cap hardening parameter; $\mathfrak{R}$ is the Rubin three-invariant reduction factor. F_c and F_f are the hardening cap and shear failure surface, respectively, which can be further expressed as

$$F_f(J_1) = \alpha - \lambda \exp^{-\beta J_1} + \theta J_1 \tag{32}$$

$$F_c(J_1, k) = 1 - \frac{[J_1 - L(k)][|J_1 - L(k)| + J_1 - L(k)]}{2[X(k) - L(k)]^2} \tag{33}$$

where α, β, λ, and θ are the fitting parameters of the tri-axial compressive strength of the cylindrical sample. $X(\kappa)$ is the parameter of the cap contract. $L(\kappa)$ restrains the cap from retracting past its initial location at k_0. k_0 is the value of J_1 at the initial intersection of the cap and shear surface before hardening is engaged. To verify whether the CSCM can be used for characterising the dynamic mechanical properties of hard rocks with the initial stress, the cylindrical granite specimen of
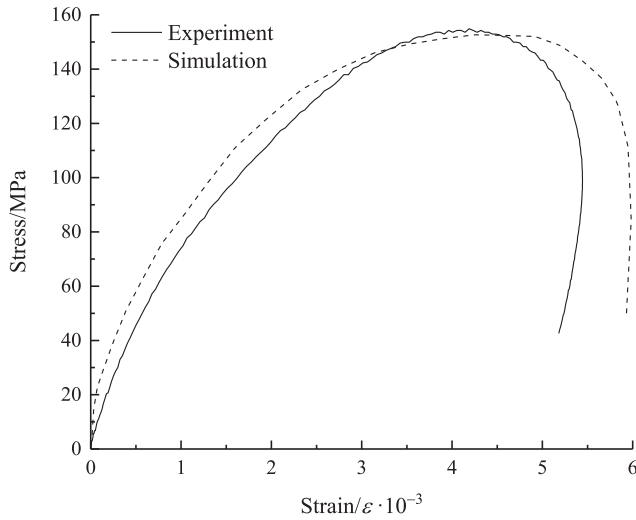
Fig. 7. Stress–strain curves obtained experimentally and numerically.

size of $\Phi 50$ mm $\times$ 100 mm is first polished. The static characteristics of the granite specimens are tested on a servo-controlled testing system, MTS-322. The dynamic strength under a static axial load is obtained based on the split Hopkinson pressure bar that is improved by researchers at the Central South University, China. The axial static and dynamic loads are 30 MPa and 200 MPa, respectively. The primary properties of the granite rock are as follows: Poisson ratio of 0.23, density of 2640 kg/m, P-wave velocity of 5166 m/s, Young's modulus of 44.96 GPa, uniaxial compression of 120.7 MPa, and uniaxial dynamic strength of 154 MPa. Furthermore, a three-dimensional (3D) numerical simulation experiment was performed according to the experimental loading conditions. The stress–strain curves obtained experimentally and numerically are shown in Fig. 7. It shows that the dynamic stress–strain curve obtained from the numerical simulation is consistent with the experimental results, especially the peak strength of the sample. Therefore, the CSCM can effectively characterise the dynamic mechanical properties of rocks.

4.3. Numerical simulation schemes of coupled static-dynamic loading

To realise the coupling simulation tests of the dynamic load and initial geostress, the implicit to explicit sequential solution method of LS-DYNA is adopted. The physical dimensions of the model used for the numerical simulation is 30 m $\times$ 20 m $\times$ 2 m, and the radius of the circular hole is 1.0 m, as shown in Fig. 8(a). The upper (Y-direction), left (X-direction), and front (Z-direction) boundaries of the model are set as the initial stress boundaries, and the lower, right, and back boundaries are set as displacement-constrained boundaries, as shown in Fig. 8(b)–(c). The semi-sine dynamic stress wave is applied to the left boundary of the model, and the loading area of the plane P-wave model is the entire left boundary, while the loading area of the cylindrical P-wave model is a rectangle of size 2 m $\times$ 1 m. In addition, to avoid the influence of the reflected wave from the stress boundary, the circular hole is set at the point where the distance to the stress boundaries and displacement-constrained boundaries in the X and Y directions are 10 m, 20 m, 10 m, and 10 m, respectively.

The numerical experiment is divided into two steps. The first step is to construct the stress environment of the underground cavity through the implicit calculation of LS-DYNA, and the stress state of every element as well as node under the initial stress is written in *dynain*, which is generated in the implicit calculation. The second part is to use the application of explicit calculation to realise the coupling calculation of dynamic stress and initial static load. The key step in the explicit calculation is to add the key words for the explicit calculation, and input *dynain* into the file that included all the information regarding the

model after deleting the duplicated elements and nodes. The initial stress conditions and dynamic loading stress P_D are as follows:

(1) $\gamma = 0.5$; $P_Z = 50$ MPa, $P_Y = 60$ MPa, $P_X = 30$ MPa; $P_D = 200$ MPa
(2) $\gamma = 1.0$; $P_Z = 50$ MPa, $P_Y = 30$ MPa, $P_X = 30$ MPa; $P_D = 200$ MPa
(3) $\gamma = 1.5$; $P_Z = 50$ MPa, $P_Y = 30$ MPa, $P_X = 45$ MPa; $P_D = 200$ MPa.

As presented in Section 3, a significant difference is found from the DSCFs around the circular cavity, which is subjected to plane and cylindrical P-waves under different loading conditions. To further study the macroscopic mechanical response around the circular cavity under an initial stress coupled with a dynamic disturbance, the process of dynamic failure as well as the effects of period and initial pressure coefficients under plane and cylindrical P-waves is simulated numerically based on the CSCM.

5. Numerical simulation of underground tunnel subjected to plane and cylindrical waves

5.1. Plastic deformation and failure

Fig. 9 presents the processes of plastic deformation and failure around the circular hole under the action of the plane P-wave. The period of the stress wave is 200 ms, and the initial static pressure coefficient P_X/P_Y is 1.0. As shown, the slight plastic deformation first occurs in the compressive stress concentration areas at the top and bottom (near $\theta = \pi/2$ and $\theta = 3\pi/2$) of the circular cavity when $T = 3184$ μs. With the continuous action of stress waves, the extent and scope of plastic deformation at the top and bottom of the circular cavities increase gradually, and the plastic failure appears at $T = 3391$ μs. Until $T = 4484$ μs, a large range of plastic deformation occurs at the top of the circular cavity, and plastic deformation is shown in the tensile stress concentration areas at the two sides of the circular cavity. Meanwhile, the plastic deformation on the illuminated side ($\theta = \pi$) is greater than that on the shadow side ($\theta = 0$). The plastic deformation in the tensile stress concentration area will further develop into a plastic failure zone under the sustained action of the stress wave, while the range of plastic deformation and failure in the compressive stress concentration area will no longer continue to increase after the plastic deformation occurs in the tensile stress concentration area. This phenomenon is considered from the perspective of energy, in that the plastic deformation and failure in the tensile stress concentration area induce the migration of the energy assembled around the cavity towards to the tensile stress concentration area. When $T = 5787$ μs, a large range of plastic failure occurs in the tensile stress concentration area around the circular cavity, and the scope of plastic failure on the illuminated side is greater than that on the shadow side. In addition, the obvious plastic deformation can be found in other positions around the circular cavity with the increase in plastic failure in the compressive and tensile stress concentration areas.

Fig. 10 shows the steps of plastic deformation and failure around the circular hole under the action of the cylindrical P-wave. The period of the stress wave and the initial static pressure coefficient P_X/P_Y are 200 ms and 1.0, respectively. The distance between the wave source and the circular tunnel r_0 is 5a. Fig. 10 shows that a small range of plastic deformation first appear in the vicinity of the illuminated side of the circular hole under the action of the cylindrical P-wave when $T = 1887$ μs, and it gradually evolves into plastic failure when $T = 2078$ μs. With the continuous action of stress wave, the plastic deformation and failure in the illuminated side extends gradually along the radial direction of the hole. The plastic deformation in the shadow side occurs at $T = 2692$ μs and the slight plastic failure appears at $T = 2998$ μs. The scope of plastic failure increases little on the illuminated side, while the range of plastic deformation, especially the plastic deformation around the top and bottom of the circular hole, increase gradually with increasing T. Obvious plastic failure occurs in the two
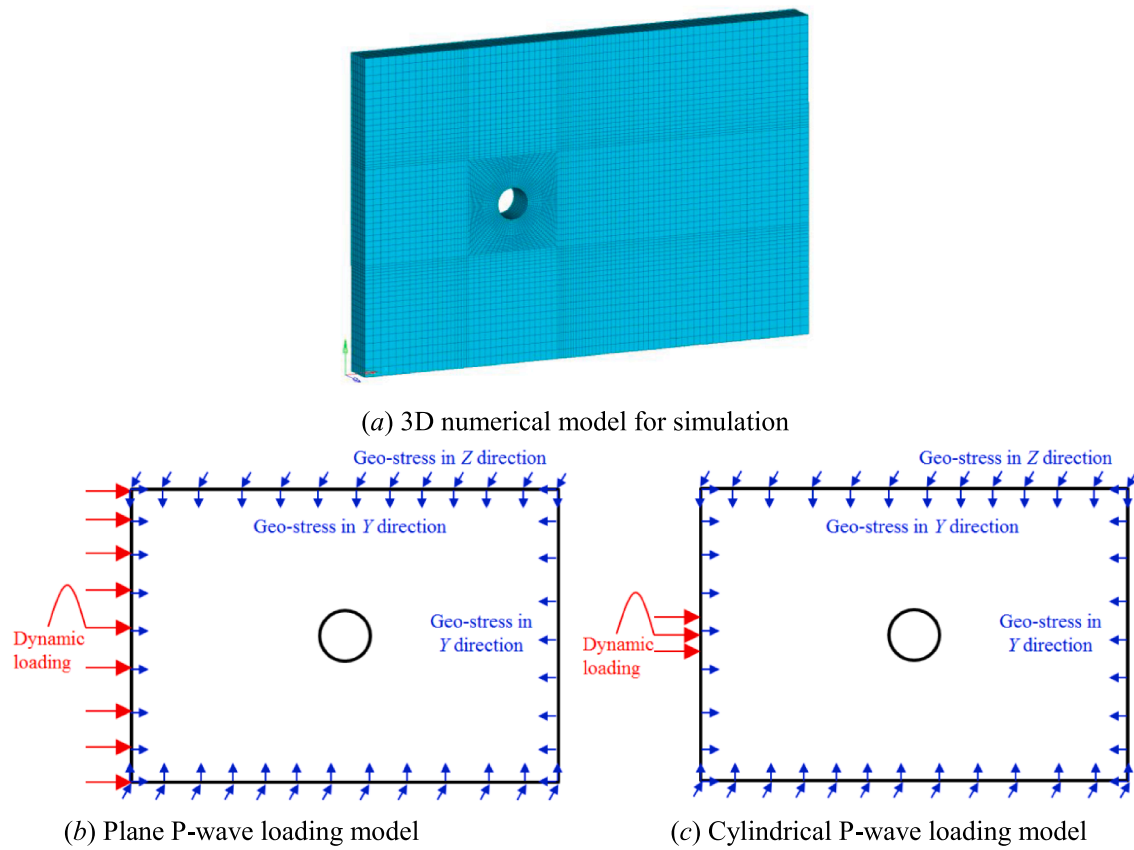
(*a*) 3D numerical model for simulation

(*b*) Plane P-wave loading model   (*c*) Cylindrical P-wave loading model

Fig. 8. 3D numerical model and loading model for simulation experiments.

T = 3184 μs T = 3391 μs T = 3791 μs

T = 4484 μs T = 4795 μs T = 5787 μs
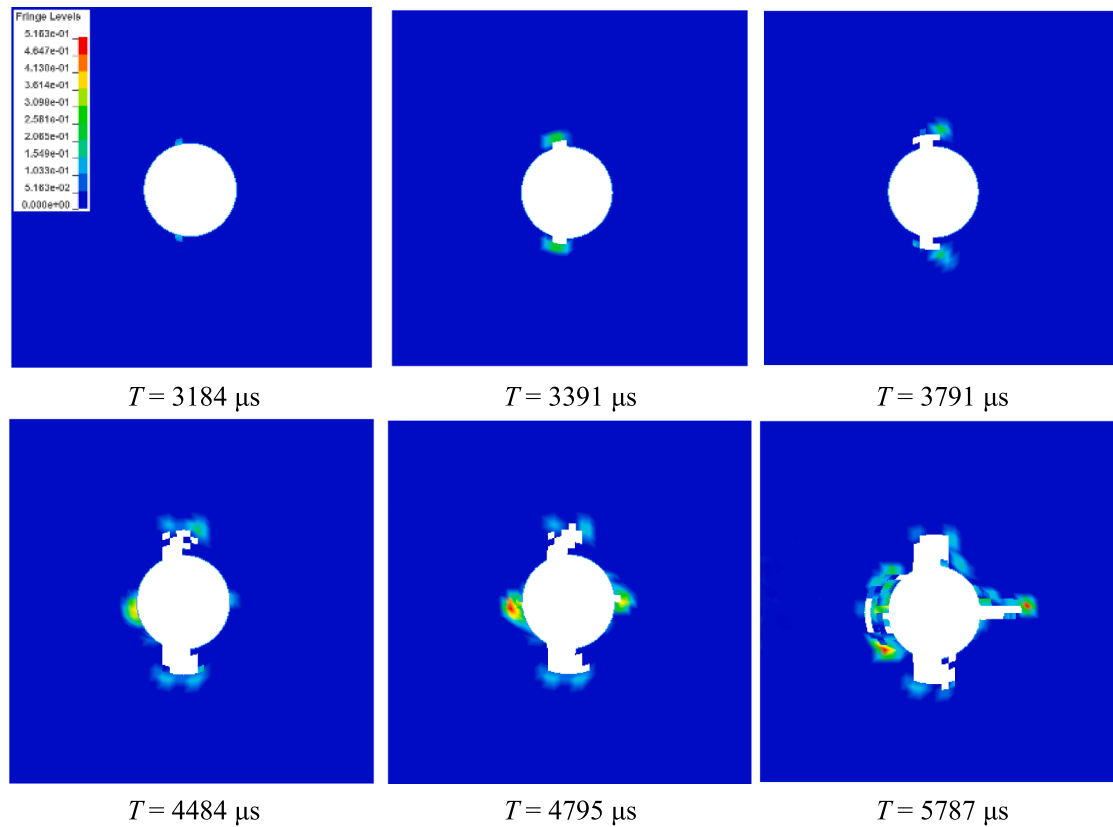
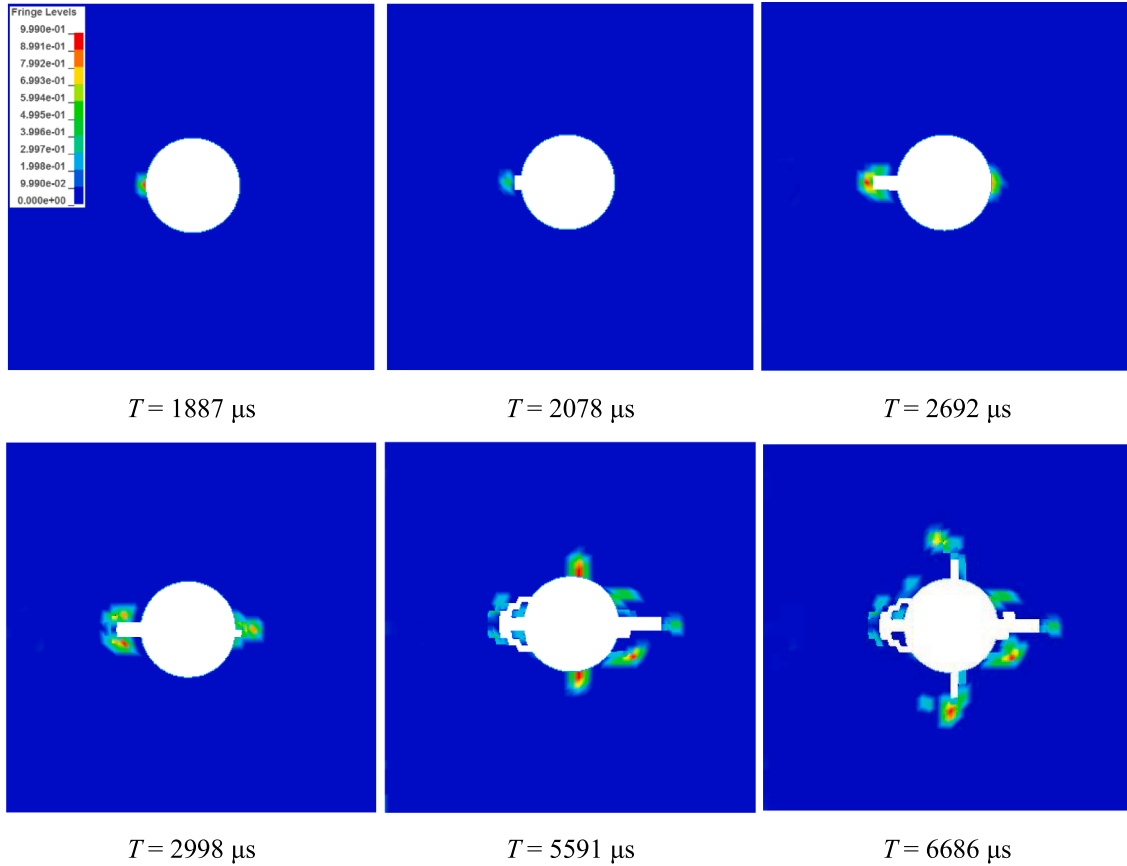**Fig. 9.** Processes of plastic deformation and failure around the circular hole under plane *P*-wave.

Fig. 10. Processes of plastic deformation and failure around circular hole under cylindrical *P*-wave.

sides of the circular hole when *T* increases to 5591 μs, and the distribution of plastic failure around the circular is highly similar to that caused by the cylindrical *P*-wave. Significant plastic deformation can be found nearby the compressive stress concentration area, and it develops gradually into plastic failure at *T* = 6686 μs. In addition, it is interesting that the position of plastic deformation returned gradually to the middle position of the top and bottom of the roadway after plastic failure occurs at the compressive stress concentration area around the circular hole, which is consistent with the variation trends in the results obtained from theoretical calculations.

5.2. Influence of period

To investigate the influence of the period on the dynamic response around the circular cavity, the dynamic stress with period of 200 ms, 40 ms, and 10 ms is further simulated. The initial static pressure coefficient P_X/P_Y is 1.0. The final plastic failure characteristics in the vicinity of a circular cavity under the plane *P*-wave and cylindrical *P*-wave is presented in Fig. 11. As shown, the plastic failure level under the plane *P*-wave decreases with decreasing t_0, which is similar to the case under the cylindrical *P*-wave. Among them, the serious dynamic damage around the circular hole, including the damage in the compressive and tensile stress concentration areas, occurs at $t_0 = 200$ ms. When $t_0 \leq 40$ ms, plastic deformation and failure appears only at the illuminated side of the circular cavity. This is because the shorter the rising time, the higher is the frequency corresponding to the stress wave. According to the relationship between the frequency and attenuation of the stress wave, a stress wave with a high frequency is easier to attenuate than a low-frequency stress wave in the processes of propagation that will cause the rapid dissipation of energy propagated in the stress wave. Therefore, the shorter the rising time t_0, the less is the residual strain energy when the stress wave propagates through the

periphery of the cavity. Moreover, we found that the obvious tensile deformation and failure are caused primarily by the stress wave with a short rising time ($t_0 \leq 40$ ms), indicating that the slabbing failure occurs only when the rising time t_0 reaches a critical value. The scope of plastic deformation and failure caused by the plane wave is larger than that caused by the cylindrical wave when $t_0 \leq 40$ ms.

5.3. Influence of initial static lateral pressure coefficient

Fig. 12 presents the failure characteristics around the circular cavity caused by the plane and cylindrical *P*-waves under different initial static coefficients. The obvious difference in the failure characteristics was caused by the two types of stress waves under different initial lateral pressure coefficients. Under a plane *P*-wave, the plastic failure occurs primarily in the roof and floor of the circular hole when the initial static pressure coefficient γ is 0.5, and two small symmetrical plastic deformations in the vicinity of the failure areas can be found in the illuminated side of the circular cavity. With the increase in the initial static pressure coefficient, severe plastic damage occurs in the two sidewalls and extends along the radial direction of the cavity. Further, the scope of damage near the roof and floor has a slight decrease when γ is 1.5. Under a cylindrical wave, obvious plastic failures occur in the two sides of the circular cavity and slight plastic failures occur symmetrically in the vicinity of the roof and floor when γ is 0.5. Serious plastic failure, including the failures in the sidewalls, roof, and floor, occurs at γ = 1.0. The damage level in the sidewalls increases significantly while only a slight plastic deformation appears in the roof and floor at γ = 1.5, which is similar to the case caused by the plane *P*-wave. This is because the roof and floor of the circular cavity are tensile stress concentration areas, and the sidewalls are compressive stress concentration areas when γ is less than 1.0; therefore, the tensile and compressive strains are stored in the tensile and compressive stress

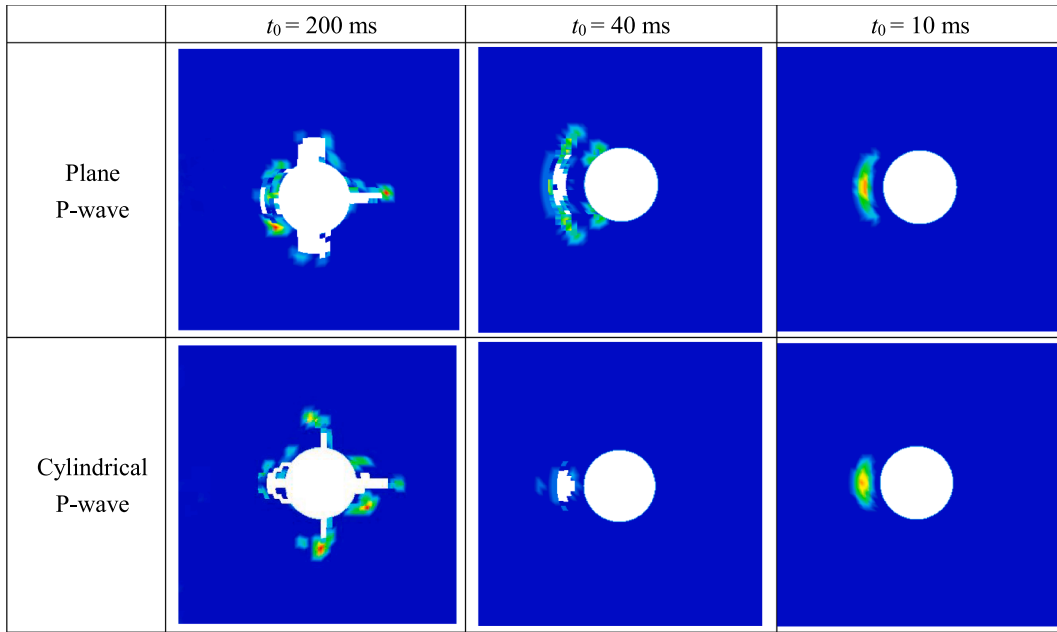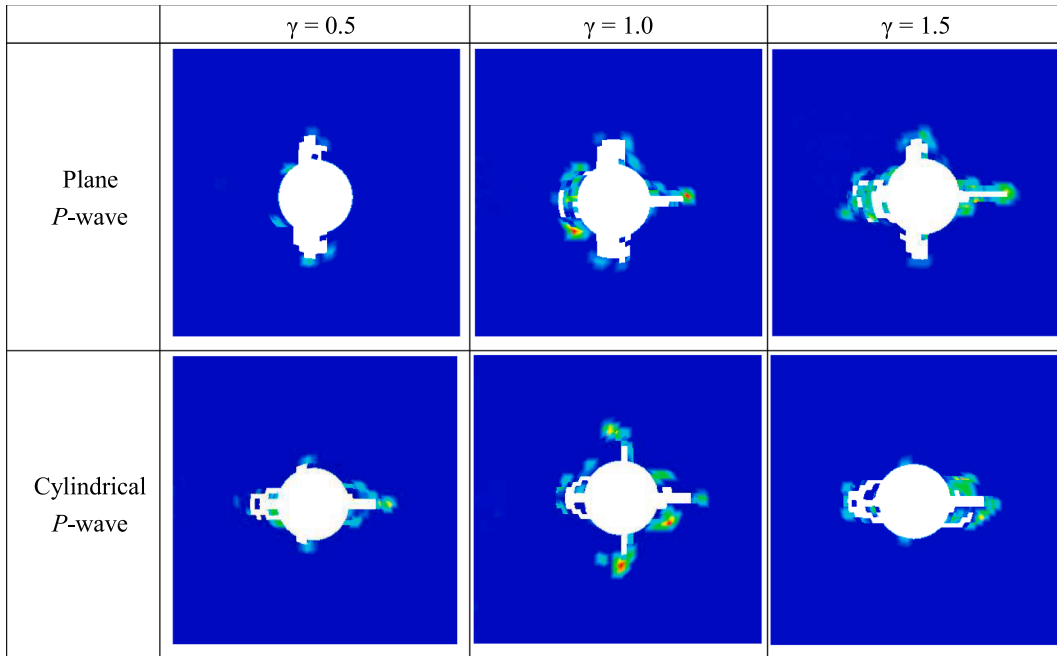**Fig. 11.** Influences of period on plastic deformation and failure.

Fig. 12. Influences of the initial static pressure coefficient on plastic deformation and failure.

concentration areas, respectively. The energy of the stress wave will overlap with the energy in the tensile stress concentration areas to trigger more serious dynamic failures. However, the energy of the stress wave will counteract with the energy in the compressive areas, thus reducing the damage in the sidewalls. Similarly, the failure in the opposite direction around the circular cavity is found when γ is larger than 1.0, indicating that the failure around the circular hole is associated significantly with the lateral pressure coefficient and incident direction.

6. Discussion

The previous analysis presents that the dynamic response around the circular cavity is significantly different under the action of plane and cylindrical P-waves. Specifically, we further analysed the

characteristics of stress variation and distribution as well as the influencing factors around the circular cavity. The theoretical results indicate that the DSCFs induced by the plane P-wave are distributed axisymmetrically around the circular hole, while the DSCFs caused by the cylindrical P-wave are distributed symmetrically along the incident direction of the dynamic stress wave. Furthermore, the maximum compressive stress concentration areas incline to the illuminated side. The magnitude of the dynamic stress concentration under the cylindrical P-wave is larger than that caused by the plane P-wave, especially with regard to the tensile stress concentration. In the previous findings presented by Moon and Pao (1967), the distribution characteristics of steady-state DSCFs around the circular cavities under spherical waves were similar to that under plane waves, distributing symmetrically at approximately $\theta = \pm \pi/2$, when the distance between the cavity and
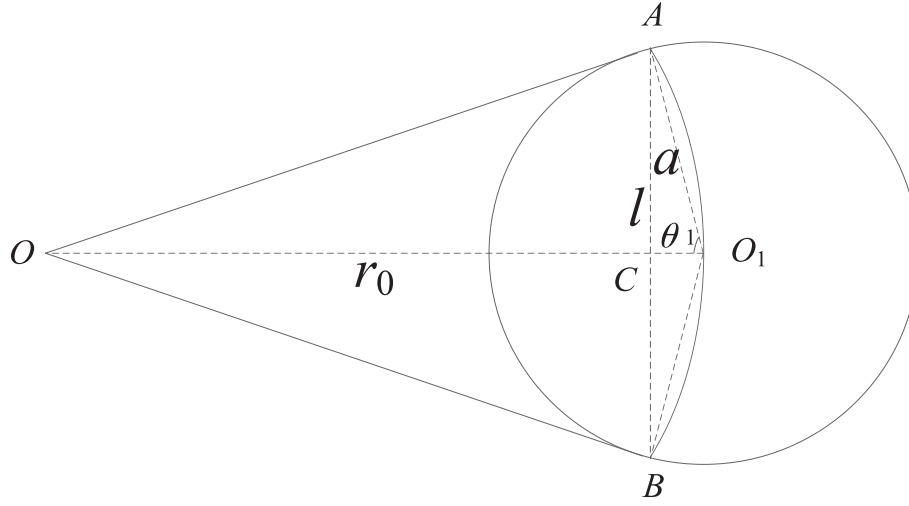
Fig. 13. Schematic diagram of the geometric relationship between wavefront and circular hole.

wave sources was large and the wave number was small. The DSCFs at $\theta = 70°$ under the spherical waves is greater than that at $\theta = \pi/2$, indicating that the stress concentration areas are distributed primarily in the illuminated side. These results indicate that the curvature of the wavefront can affect the DSCFs and its distribution around the circular hole significantly.

In general, the curvature of the stress wavefront is a relative value. When the size of the excavation span is large and the location is close to the wave source, the curvature of the incident wave passing through the circular hole is large. Thus, the incident stress wave can be considered as a cylindrical wave. However, as the distance between the cavity and wave source increases, the curvature of the wavefront decreases gradually, and the incident stress wave can be approximated as a plane wave when the stress acts on the circular hole. In addition, the plane P-wave and cylindrical P-wave may occur at both the near and far source locations when the size of the excavation span changes with the distance. Therefore, the curvature of the incident wave is related to the distance between the wave source and cavity, as well as the excavation span of the hole. Thus, to further analyse the relationship between the distances from the wave source to the excavation, the excavation span of the cavity is key to distinguish between the plane P-wave and cylindrical P-wave. According to the geometric relationship between the incident wave and the excavation span of the cavity, the wavefront of the incident wave can be regarded as an arc, as shown in Fig. 13. As shown, the wavefront can be approximated as a plane when the value of θ_1 approaches $\pi/2$. Thus, according to the geometry of a triangle, the corresponding chord length l of the incident wavefront curve can be expressed as

$$l = 2a \cdot \sin\theta_1 \tag{34}$$

where $\theta_1 = \arccos\frac{a}{r_0}$. To obtain the critical value of the plane P-wave and cylindrical P-wave, we can make l tend infinitely to 2a ($l \to 2a$) and obtain

$$\arccos\frac{a}{r_0} \to \frac{\pi}{2} \tag{35}$$

Eq. (35) is the critical expression of the plane P-wave and cylindrical P-wave. However, θ_1 can only be an acute angle that is infinitely close to $\pi/2$ based on the properties of a triangle. Based on formula (35), the relationship between the excavation span of the cavity (a), the distance from the wave source to the centre of the cavity (r_0), and the average curvature of the incident wave ($\bar{K}$) is presented in Fig. 14. As shown, the curvature of the incident wave decreases rapidly as r_0 increases at $r_0 < 10a$, and changes slowly when $r_0 > 10a$, indicating that the influence of its curvature on the dynamic response around the cavity is
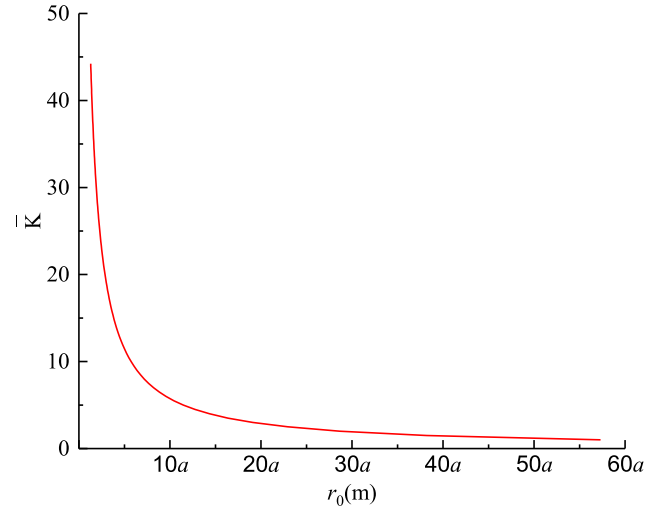

Fig. 14. Relationship among curvature $\bar{K}$, distance r_0, and excavation span a.
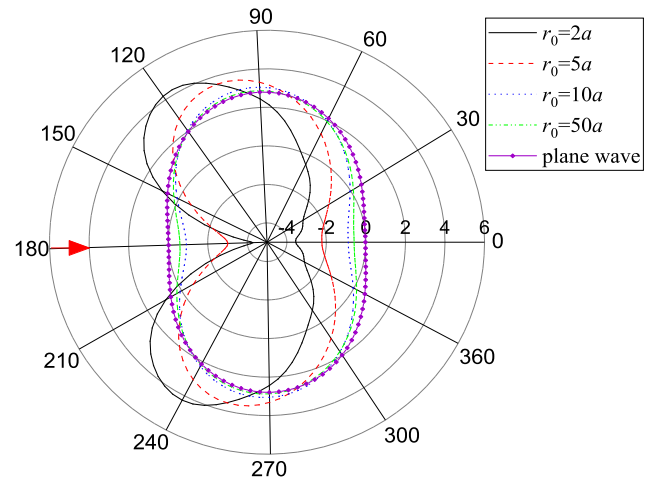

Fig. 15. Dynamic stress concentration distribution characteristics caused by cylindrical wave at different r_0.

reduced gradually.

Fig. 15 presents the DSCFs caused by the cylindrical P-wave at different wave source distances r_0. As shown, the compressive stress concentration factors are distributed primarily towards to the

illuminated side when r_0 is small. The compressive stress concentration factors shift gradually towards to the centre of the top and bottom of the hole ($\theta = \pi/2$ and $\theta = 3\pi/2$, respectively) with the increase in r_0, and gradually distributes symmetrically along the incident direction and the direction of $\theta = \pm \pi/2$, which is similar to that caused by the plane P-wave. Meanwhile, the compressive and tensile stress concentration factors decrease with increasing r_0, and the level of stress concentration gradually approach towards that induced by the plane P-wave when $r_0 > 10a$, which is consistent with the results obtained from Fig. 13. Therefore, $r_0 = 10a$ can be considered as the critical value for distinguishing plane waves from cylindrical waves, namely, the incident wave can be approximated as a plane wave when $r_0 > 10a$; otherwise, it is a cylindrical wave.

In addition, we further simulated the entire process of the scattering of the plane stress wave and cylindrical stress wave around the circular hole, considering the effects of initial geostress, period, and lateral pressure coefficients. The results of the simulations are consistent with the theoretical results. The plastic deformations and failures under the plane wave first occurred at the roof and floor of the circular hole, and subsequently occurred at its two sidewalls, which is completely opposite to that under the cylindrical stress wave. Li et al. (2018) and Li and Weng (2016) studied the dynamic response around the vertical wall arch and circular roadway under a triangular plane stress wave, indicating that the dynamic response is related to the initial lateral pressure coefficient and incidence direction. Their results indicated that when the lateral pressure coefficient is greater than 1.0, the failure occurred primarily in the roof and floor of the roadway owing to the high strain energy caused by the initial compressive stress concentration. However, when the lateral pressure coefficient is less than 1.0, the failure position is consistent with the direction of the incident stress wave, and the failure type is dynamic spalling. Moreover, other studies indicated that the dynamic response of the underground tunnel was related strongly with the ratio of the incident wavelength to the excavation span (λ/D) (Chen et al., 2012; Li et al., 2018; Wang et al., 2014; Wang and Cai, 2015; Zhu et al., 2010). For example, Zhu et al. (2010) obtained the dynamic damage characteristics around a circular tunnel when the ratio (λ/D) was less 1.0, indicating that the dynamic failures appeared primarily in the incident side. Similarly, Li et al. (2018) indicated that the dynamic failure appeared primarily in the roof and floor when the ratio was 1.5. As described in the presented study, the conclusions were consistent with their results. Additionally, the influence of the wavefront curvature on the dynamic failure characteristics around the opening is an important factor that cannot be ignored based on previous analyses and discussions. Hence, the numerical results with different loading areas, which are used primarily for generating incident waves with different wavefront curvatures, is presented in Fig. 16. As shown, the damage around the circular cavity develops gradually from the sidewalls to the roof and floor as the loading area increases. This indicates that the smaller the wavefront curvature relative to the circular hole, the easier it is for the hole to be damaged in the roof and floor. Therefore, the strengthened support structure should be designed in the underground cavity, especially in the tensile stress concentration areas when the source of disturbance is close to the underground cavity. The theoretical range for the strengthened support structure is approximately $10a$.

7. Conclusions

In the present study, the numerical solutions of the dynamic stress concentration around a circular cavity subjected to plane and cylindrical P-waves is first presented based on the wave function expansion methods and Fourier transform. In addition, the dynamic failure characters under the plane P-wave and cylindrical P-wave is subsequently investigated by the finite element software LS-DYNA. The results indicate that the wavefront curvature of the incident stress wave present significant effects on the dynamic response of a circular cavity. The DSCFs under the plane P-wave is distributed systematically at $\theta = 0–\pi$ and $\theta = \pi/2–3\pi/2$, where the tensile and compressive stress concentrations are generated, and the compressive stress concentration level is much larger than the tensile stress concentration level. The DSCFs caused by the cylindrical P-wave distributed along $\theta = 0–\pi$ systematically, and the stress concentration level is larger than that caused by the plane P-wave, especially the tensile stress concentration factors. Moreover, the numerical simulations indicate that the dynamic failure occurs initially at the roof and floor of the cavity under the plane P-wave, while the dynamic failure first appears at the illuminated sidewall under the cylindrical P-wave. Furthermore, the dynamic response caused by the cylindrical P-wave become gradually similar to the plane P-wave as the distance between the wave source and cavity r_0 increases when the size of the cavity a was constant, and the plane P-wave can be approximated as a cylindrical P-wave when r_0 increases to greater than $10a$. More specifically, the smaller the wavefront curvature relative to the circular hole, the easier it is for the hole to be damaged in the roof and floor. This study provides meaningful information relevant to underground mining and tunnel design, construction, and support processes.

Loading area: 2 m × 1 m   Loading area: 2 m × 2 m   Loading area: 2 m × 5 m   Plane wave
$T = 2998$ μs $T = 2994$ μs $T = 2990$ μs $T = 3791$ μs

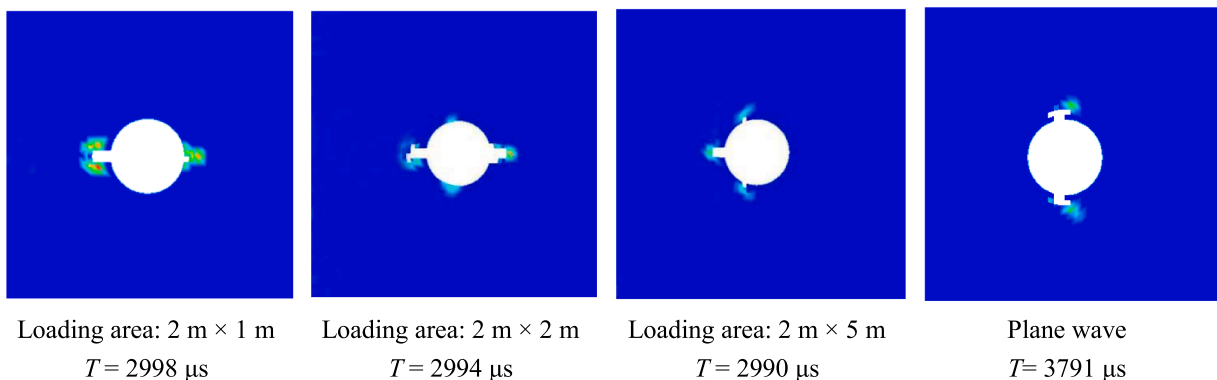**Fig. 16.** Failure characteristics around the circular hole under different wavefront curvature.

Appendix A

$$\varepsilon_{11}^{(1)} = [n^2 + n - (\beta r)^2/2]J_n(\alpha r) - \alpha r J_{n-1}(\alpha r)$$

$$\varepsilon_{11}^{(3)} = [n^2 + n - (\beta r)^2/2]H_n^{(1)}(\alpha r) - \alpha r H_{n-1}^{(1)}(\alpha r)$$

$$\varepsilon_{12}^{(3)} = -n(n+1)H_n^{(1)}(\beta r) + n\beta r H_{n-1}^{(1)}(\beta r)$$

$$\varepsilon_{21}^{(1)} = -[n^2 + n - (\beta r)^2/2 - (\alpha r)^2]J_n(\alpha r) + \alpha r J_{n-1}(\alpha r)$$

$$\varepsilon_{21}^{(3)} = -[n^2 + n - (\beta r)^2/2 - (\alpha r)^2]H_n^{(1)}(\alpha r) + \alpha r H_{n-1}^{(1)}(\alpha r)$$

$$\varepsilon_{22}^{(3)} = n(n+1)H_n^{(1)}(\beta r) - n\beta r H_{n-1}^{(1)}(\beta r)$$

$$\varepsilon_{41}^{(1)} = n(n+1)J_n(\alpha r) - n\alpha r J_{n-1}(\alpha r)$$

$$\varepsilon_{41}^{(3)} = n(n+1)H_n^{(1)}(\alpha r) - n\alpha r H_{n-1}^{(1)}(\alpha r)$$

$$\varepsilon_{42}^{(3)} = -[n^2 + n - (\beta r)^2/2]H_n^{(1)}(\beta r) + \beta r H_{n-1}^{(1)}(\beta r)$$

References

Brannon, R.M., Leelavanichkul, S., 2009. Survey of Four Damage Models for Concrete. Prod.sandia.gov.

Chen, Z.Y., Chen, S., Li, T.B., Yuan, Y., 2012. Damage characteristics and influence factors of mountain tunnels under strong earthquakes. Nat. Hazards 61, 387–401.

Deng, X.F., Zhu, J.B., Chen, S.G., Zhao, Z.Y., Zhou, Y.X., Zhao, J., 2014. Numerical study on tunnel damage subject to blast-induced shock wave in jointed rock masses. Tunn. Undergr. Space Technol. 43, 88–100.

Fang, X.Q., Jin, H.X., 2017. Dynamic response of a non-circular lined tunnel with visco-elastic imperfect interface in the saturated poroelastic medium. Comput. Geotech. 83, 98–105.

Fang, X.Q., Jin, H.X., Wang, B.L., 2015. Dynamic interaction of two circular lined tunnels with imperfect interfaces under cylindrical P-waves. Int. J. Rock Mech. Min. Sci. 79, 172–182.

Feng, G.L., Feng, X.T., Chen, B.R., Xiao, Y.X., Yu, Y., 2015. A Microseismic method for dynamic warning of rockburst development processes in tunnels. Rock Mech. Rock Eng. 48, 2061–2076.

Golshani, A., Oda, M., Okui, Y., Takemura, T., Munkhtogoo, E., 2007. Numerical simulation of the excavation damaged zone around an opening in brittle rock. Int. J. Rock Mech. Min. Sci. 44, 835–845.

Hauksson, E., Jones, L.M., 1989. The 1987 Whittier Narrows earthquake sequence in Los Angeles, southern California: Seismological and tectonic analysis. J. Geophys. Res. Solid Earth 94, 9569–9589.

Huang, J.Q., Zhao, M., Du, X.L., 2017. Non-linear seismic responses of tunnels within normal fault ground under obliquely incident P waves. Tunn. Undergr. Space Technol. 61, 26–39.

Jeon, S., Kim, J., Seo, Y., Hong, C., 2004. Effect of a fault and weak plane on the stability of a tunnel in rock—a scaled model test and numerical analysis. Int. J. Rock Mech. Min. Sci. 41, 486-486.

Jiang, Q., Feng, X.T., Chen, J., Huang, K., Jiang, Y.L., 2013. Estimating in-situ rock stress from spalling veins: a case study. Eng. Geol. 152, 38–47.

Jing, L., 2003. A review of techniques, advances and outstanding issues in numerical modelling for rock mechanics and rock engineering. Int. J. Rock Mech. Min. Sci. 40, 283–353.

Kouretzis, G.P., Andrianopoulos, K.I., Sloan, S.W., Carter, J.P., 2014. Analysis of circular tunnels due to seismic P-wave propagation, with emphasis on unreinforced concrete liners. Comput. Geotech. 55, 187–194.

Labiouse, V., Vietor, T., 2014. Laboratory and in situ simulation tests of the excavation damaged zone around galleries in opalinus clay. Rock Mech. Rock Eng. 47, 57–70.

Li, X.B., Cao, W.Z., Tao, M., Zhou, Z.L., Chen, Z.H., 2016. Influence of unloading disturbance on adjacent tunnels. Int. J. Rock Mech. Min. Sci. 84, 10–24.

Li, X.B., Cao, W.Z., Zhou, Z.L., Zou, Y., 2014. Influence of stress path on excavation unloading response. Tunnel. Undergr. Space Technol. Incorpor. Trench. Technol. Res. 42, 237–246.

Li, X.B., Li, C.J., Cao, W.Z., Tao, M., 2018. Dynamic stress concentration and energy evolution of deep-buried tunnels under blasting loads. Int. J. Rock Mech. Min. Sci. 104, 131–146.

Li, X.B., Weng, L., 2016. Numerical investigation on fracturing behaviors of deep-buried opening under dynamic disturbance. Tunnel. Undergr. Space Technol. Incorpor. Trench. Technol. Res. 54, 61–72.

Lisjak, A., Grasselli, G., Vietor, T., 2014. Continuum–discontinuum analysis of failure mechanisms around unsupported circular excavations in anisotropic clay shales. Int. J. Rock Mech. Min. Sci. 65, 96–115.

Liu, Q.J., Zhao, M.J., Wang, L.H., 2013. Scattering of plane P, SV or Rayleigh waves by a shallow lined tunnel in an elastic half space. Soil Dyn. Earthquake Eng. 49, 52–63.

Liu, Z.X., Ju, X., Wu, C.Q., Liang, J.W., 2017. Scattering of plane P1 waves and dynamic stress concentration by a lined tunnel in a fluid-saturated poroelastic half-space. Tunn. Undergr. Space Technol. 67, 71–84.

Liu, Z.X., Sun, S.J., Alexander, H.D., C., W, Y.R., 2018a. A fast multipole accelerated indirect boundary element method for broadband scattering of elastic waves in a fluid-saturated poroelastic domain. Int. J. Numer. Anal. Methods Geomech., pp. 1–28.

Liu, Z.X., Wang, Z.K., AHD, C., L, J.W., W, C.C., 2018b. The method of fundamental solution for 3-D wave scattering in a fluid: aturated poroelastic infinite domain. Int. J. Numer. Anal. Meth. Geomech. 42, 1866–1889.

LSTC, 2007. LS-DYNA Keyword User's Manual, Version 971. Livermore Software Technology Corporation, Livermore.

Lu, W.B., Yang, J.H., Yan, P., Chen, M., Zhou, C.B., Luo, Y., Jin, L., 2012. Dynamic response of rock mass induced by the transient release of in-situ stress. Int. J. Rock Mech. Min. Sci. 53, 129–141.

Mi, C.W., Kouris, D., 2013. Stress concentration around a nanovoid near the surface of an elastic half-space. Int. J. Solids Struct. 50, 2737–2748.

Moon, F.C., Pao, Y.H., 1967. The influence of the curvature of spherical waves on dynamic stress concentration. J. Appl. Mech. 34, 373–379.

Pao, Y.H., Mow, C.C., 1973. Diffraction of Elastic Waves and Dynamic Stress Concentrations. Crane, Russak & Company. Inc., New York, pp. 601–612.

Pao, Y.H., Mow, C.C., 1993. Scattering and Dynamics Stresses Concentration of Elastic Wave. Science Press, Beijing.

Sezawa, K., 1927. Scattering of elastic waves and some applied problems. Bull. Earthquake Res. Inst. 1927, pp. 1–9.

Su, G.S., Feng, X.T., Wang, J.H., Jiang, J.Q., Hu, L.H., 2017. Experimental study of remotely triggered rockburst induced by a tunnel axial dynamic disturbance under true-triaxial conditions. Rock Mech. Rock Eng. 1–20.

Tao, M., Li, X.B., Wu, C.Q., 2012. Characteristics of the unloading process of rocks under high initial stress. Comput. Geotech. 45, 83–92.

Tao, M., Li, Z.W., Cao, W.Z., Li, X.B., Wu, C.Q., 2019. Stress redistribution of dynamic loading incident with arbitrary waveform through a circular cavity. Int. J. Numer. Anal. Methods Geomech.

Tao, M., Zhao, H.T., Li, X.B., Li, X., Du, K., 2018. Failure characteristics and stress distribution of pre-stressed rock specimen with circular cavity subjected to dynamic loading. Tunn. Undergr. Space Technol. 81, 1–15.

Wang, T.T., Hsu, J.T., Chen, C.H., Huang, T.H., 2014. Response of a tunnel in double-layer rocks subjected to harmonic P- and S-waves. Int. J. Rock Mech. Min. Sci. 70, 435–443.

Wang, W.L., Wang, T.T., Su, J.J., Lin, C.H., Seng, C.R., Huang, T.H., 2001. Assessment of damage in mountain tunnels due to the Taiwan Chi-Chi Earthquake. Tunnel. Undergr. Space Technol. Incorpor. Trench. Technol. Res. 16, 133–150.

Wang, X., Cai, M., 2015. Influence of wavelength-to-excavation span ratio on ground motion around deep underground excavations. Tunnel. Undergr. Space Technol. Incorpor. Trench. Technol. Res. 49, 438–453.

Wang, Z.Z., Gao, B., Jiang, Y.J., Yuan, S., 2009. Investigation and assessment on mountain tunnels and geotechnical damage after the Wenchuan earthquake. Sci. China 52, 546–558.

Xiao, Y.X., Feng, X.T., Feng, G.L., Liu, H.J., Jiang, Q., Qiu, S.L., 2016. Mechanism of evolution of stress–structure controlled collapse of surrounding rock in caverns: a case study from the Baihetan hydropower station in China. Tunnel. Undergr. Space Technol. Incorpor. Trench. Technol. Res. 51, 56–67.

Yan, X., Kulatilake, P.H.S.W., Sandbak, L.A., 2018. Effect of rock mass and discontinuity mechanical properties and delayed rock supporting on tunnel stability in an underground mine. Eng. Geol. 238, 62–75.

Yang, J.H., Lu, W.B., Jiang, Q.H., Yao, C., Jiang, S.H., Tian, L., 2016. A study on the vibration frequency of blasting excavation in highly stressed rock masses. Rock Mech. Rock Eng. 49, 2825–2843.

Yang, J.H., Lu, W.B., Chen, M., Yan, P., Zhou, C.B., 2013. Microseism induced by transient release of in situ stress during deep rock mass excavation by blasting. Rock Mech. Rock Eng. 46, 859–875.

Yang, Z.L., Zhang, C.Q., Yang, Y., Sun, B.T., 2017. Scattering of out-plane wave by a circular cavity near the right-angle interface in the exponentially inhomogeneous media. Wave Motion 72, 354–362.

Yi, C.P., Zhang, P., Johansson, D., Nyberg, U., 2014. Dynamic response of a circular lined tunnel with an imperfect interface subjected to cylindrical P-waves. Comput. Geotech. 55, 165–171.

Yi, C.P., Lu, W.B., Zhang, P., Johansson, D., Nyberg, U., 2016. Effect of imperfect interface on the dynamic response of a circular lined tunnel impacted by plane P-waves. Tunnel. Undergr. Space Technol. Incorpor. Trench. Technol. Res. 51, 68–74.

Zhu, W.C., Li, Z.H., Zhu, L., Tang, C.A., 2010. Numerical simulation on rockburst of underground opening triggered by dynamic disturbance. Tunnel. Undergr. Space

Technol. Incorpor. Trench. Technol. Res. 25, 587–599.

Zhu, W.C., Wei, J., Zhao, J., Niu, L.L., 2014. 2D numerical simulation on excavation damaged zone induced by dynamic stress redistribution. Tunnel. Undergr. Space Technol. Incorpor. Trench. Technol. Res. 43, 315–326.

Zhu, J.B., Zhou, T., Liao, Z.Y., Sun, L., Li, X.B., Chen, R., 2018. Replication of internal defects and investigation of mechanical and fracture behaviours of rocks using 3D

printing and 3D numerical methods with combination of X-ray computerized tomography. Int. J. Rock Mech. Min. Sci. 106, 198–212.

Zou, Y., Liu, H.B., Jing, L.P., Miao, Y., 2018. Response of circular tunnel with imperfect interface bonding in layered ground subjected to obliquely incident plane P or SV wave. Int. J. Numer. Anal. Meth. Geomech. 1–17.